

Research Article

Artifact Analysis for Axially Elongated Lissajous Trajectories in Magnetic Particle Imaging

Christian Kaethner* · Aileen Cordes · Annika Hänsch · Thorsten M. Buzug

Institute of Medical Engineering, Universität zu Lübeck, Lübeck, Germany

*Corresponding author, email: kaethner@imt.uni-luebeck.de

Received 28 November 2016; Accepted 6 January 2017; Published online 23 March 2017

© 2017 Kaethner; licensee Infinite Science Publishing GmbH

This is an Open Access article distributed under the terms of the Creative Commons Attribution License (<http://creativecommons.org/licenses/by/4.0>), which permits unrestricted use, distribution, and reproduction in any medium, provided the original work is properly cited.

Abstract

Magnetic Particle Imaging promises great potential for various imaging scenarios with medical purpose. In order to meet this potential, one of the key factors is that the size and the shape of the sampling area need to be adaptable to the aimed applications. An interesting approach to achieve this within medical and technical safety limits is by use of focus fields. However, even with current focus-field approaches, an enlargement in axial direction remains a challenging task. Recently, a use of an elongated sampling trajectory was proposed to address this challenge. Such an elongation can be achieved either by superimposing an orthogonal oriented linear focus field to a 2D trajectory or by an additional continuous movement in axial direction. The resulting elongated trajectory allows for a larger axial coverage of a scanned object. However, based on the physical properties of the signal generation, the elongation length needs to be limited to avoid signal loss or the occurrence of artifacts. In this work, a simulation based artifact analysis is carried out for Lissajous trajectories to determine an elongation limit that allows for both, the avoidance of signal loss and artifacts.

1. Introduction

Magnetic Particle Imaging (MPI) is a functional imaging technique based on the interaction of magnetic fields with iron based tracer materials [1]. Due to its great potential in terms of temporal and spatial resolution combined with a high sensitivity, it is a promising new approach to address a wide range of medically related problems [2–8].

In order to generate a detectable MPI signal, the magnetic tracer material is excited by an oscillating magnetic field. This field, known as a drive field, usually features a high frequency around 25 kHz and exploits the non-linear magnetization behaviour of the particles. The resulting time-varying magnetization causes an induction

of a characteristic voltage signal, which is proportional to the particle concentration. For a spatially precise detection of such a signal, the drive field is superimposed with an additional magnetic gradient field, referred to as a selection field. The selection field features a defined area, where the magnetic field values cancel each other out. This results in a field-free region, which is usually shaped as either a field-free point (FFP) [1, 9–11] or a field-free line (FFL) [12–15]. In order to cover not only a single point or line, the FFP/FFL can be moved rapidly over the entire field of view (FOV) by adapting the applied drive fields. Among others [16], the Lissajous trajectory is one of the most commonly used sampling trajectories. It is crucial that the applied magnetic fields to realize such a trajectory and the rapid FOV sampling are within

the medical limitations [17–19]. In addition to this, it is important that the FOV is of a sufficient size and is adaptable in its shape for respective medical application scenarios.

A promising approach to achieve the aforementioned FOV features is the use of focus fields [1, 20]. However, the generation of focus fields is only feasible within a limited axial range of an MPI system. This results in a limited FOV enlargement in axial direction. In order to further enlarge the FOV, the 2D movement of the FFP/FFL in a defined imaging plane of the system can be superimposed with a mechanical movement in axial direction. As shown in [21], a continuous movement results in an elongated trajectory (see Fig. 1) and allows for 3D imaging with a 2D MPI system and features the potential of an immense FOV enlargement in axial direction. A similar sampling concept was introduced in [22] and is based on the traveling wave approach [10]. The proposed concept also features a rapid and dense sampling within the aforementioned medical limitations. The chosen sampling path is comparable to an elongated version of the radial trajectory proposed in [16].

In order to ensure a homogenous coverage and to avoid signal loss and correlated effects such as the occurrence of artifacts, the elongation length, i.e. the axial distance covered by one repetition of the trajectory, needs to be chosen within a certain limit [21].

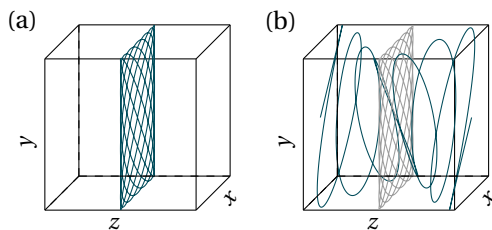


Figure 1: Example visualization of a Lissajous trajectory based data acquisition. (a) 2D planar Lissajous trajectory. (b) 2D planar Lissajous trajectory (gray) superimposed with an elongated variation (green) to sample a 3D volume.

In this work, a simulation based analysis of the elongation length for Lissajous trajectories in terms of signal loss and artifacts is performed. The aforementioned limit of the elongation length is thereby refined with a focus on neither causing signal loss nor image artifacts. Based on this, simulation experiments are carried out in order to investigate the resulting effects for different elongation lengths.

II. Theory

In order to ensure an adequate amount of acquired information by an elongated trajectory in the entire FOV, the sampling density in the direction of elongation has to be

sufficiently high. Otherwise, some particles in the FOV do not contribute significantly to the acquired signal so that an accurate reconstruction of the spatial particle distribution becomes impossible.

To define a theoretical elongation limit, the distance of each position in the FOV to the elongated trajectory has to be taken into account. The distance calculation can be carried out in various ways. One approach to estimate the amount of subsampling is given by the use of an euclidean distance measure [23]. For elongated trajectories that are based on a self-intersecting sampling path, such as a Lissajous trajectory, axial distances [21] can be used as an alternative to the euclidian ones. Due to the fact that only particles in a small region of $1X_s G_i^{-1}$ around the FFP contribute to the signal, the axial distance of each particle to the elongated trajectory should not exceed $1X_s G_i^{-1}$ to avoid signal loss [24]. Here, G_i with $i \in \{x, y, z\}$ denotes the selection-field gradient in the elongation direction and X_s is the magnetic field strength where the particle magnetization reaches half of its maximum [24]. For Lissajous trajectories, this condition is fulfilled if the elongation length is smaller than $2X_s G_i^{-1}$ [21].

However, taking into account the anisotropy of a particles signal response [25, 26], it is beneficial for the acquired signal quality to further reduce the elongation limit. In order to achieve a high spatial resolution and to strive for minimal amount of potentially occurring artifacts, the signal of each particle at a defined position should be acquired at least at two different time points with different, ideally orthogonal directions of FFP movement [16]. As a consequence, the axial distance between two points generating a self-intersection point (SIP) of the non-elongated trajectory has to be smaller than $1X_s G_i^{-1}$ to ensure that the area between these points is sampled by at least two different FFP motion directions. It follows that the elongation limit to avoid signal loss and image artifacts is approximately $1X_s G_i^{-1}$.

III. Material and Methods

III.1. Simulation Parameters

The simulations are based on the assumption of ideal magnetic fields and a suitable noise model [27]. The strength of the selection-field gradient G_i with $i \in \{x, y, z\}$ is 1.5 Tm^{-1} in the z direction and 0.75 Tm^{-1} in the x and y directions. The simulated drive-field frequencies are based on a frequency of $f_b = 2.5 \text{ MHz}$ and the frequency dividers $n_x = 93$ and $n_y = 96$. The elongation of the trajectory is simulated by use of a linear focus-field shift. The respective elongation lengths ϵ_z are chosen as $1X_s G_z^{-1}$, $1.5X_s G_z^{-1}$, $2X_s G_z^{-1}$, $3X_s G_z^{-1}$, and $4X_s G_z^{-1}$. With drive-field amplitudes of $A_i = 7.5 \text{ mT}$ with $i \in \{x, y\}$ and a maximal elongation of $4X_s G_z^{-1}$, the resulting FOV size is $10 \text{ mm} \times 10 \text{ mm} \times 4X_s G_z^{-1}$. The used

system matrices are acquired based on the same elongation lengths. The size of the respective FOV is chosen accordingly as well and it is discretized in $80 \times 80 \times 40$ sampling positions. As a sampling path for the system matrix acquisitions and the simulated measurements, an elongated Lissajous trajectory

$$\gamma(t) = \begin{pmatrix} -A_x/G_x \sin(2\pi f_b n_x^{-1} t) \\ -A_y/G_y \sin(2\pi f_b n_y^{-1} t) \\ t/T \cdot \epsilon_z \end{pmatrix} \quad (1)$$

is chosen. Here, t denotes the time and T the trajectory repetition time, which based on the chosen parameters equals 1.2 ms.

The simulation phantom consists of 9 circles that are arranged in a 3×3 grid (see Fig. 2 (a)). Each circle has a diameter of 1 mm. As example position for this analysis, the phantom is placed in the xy plane in the middle of the FOV in z direction. The center of each circle corresponds to an SIP of the chosen Lissajous trajectory [28, 29]. The circles' axial distances to the trajectory depend on the elongation length ϵ_z (see Fig. 2 (b)). For the simulation of the particle magnetization, the Langevin theory is used. The particles are assumed to consist of Magnetite and their diameters are simulated with 30 nm. According to [24], it follows that $X_s = 1.1 \text{ mT}\mu_0$.

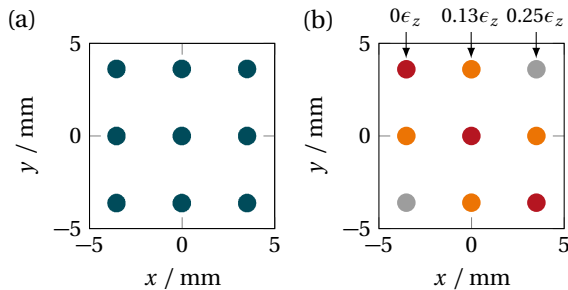


Figure 2: Visualization of the used simulation phantom. (a) The phantom consists of nine circles with a diameter of 1 mm and arranged in a 3×3 grid. (b) The circles axial distance to trajectory depends on the elongation ϵ_z .

The reconstruction of the simulated data is performed by use of an iterative Kaczmarz approach combined with a Tikhonov regularization [30].

III.II. Distance Calculation

To investigate the influence of an increasing elongation length on the resulting image quality, the computation of distances between specific segments of the trajectory and distances between the sampling path and a plane in the FOV is of great interest. The calculation of such distances can be carried out in various ways. In this contribution, axial as well as euclidean distances are taken into account.

Axial Distances

Let $\gamma'(t) = (\gamma'_x(t), \gamma'_y(t))$ be a 2D sampling path with SIPs that are defined by two time points t_1 and t_2 with $t_1 \neq t_2$ and $\gamma'(t_1) = \gamma'(t_2)$. If $\gamma'(t)$ is axially elongated in z direction, the resulting 3D trajectory is given by $\gamma(t) = (\gamma'_x(t), \gamma'_y(t), \epsilon_z t T^{-1})$, where ϵ_z denotes the elongation length. For each SIP, it follows that the axial distance between $\gamma(t_1)$ and $\gamma(t_2)$ can be calculated by

$$\Delta a_{\min} = \min \{ \Delta \epsilon_z, \epsilon_z - \Delta \epsilon_z \} \quad (2)$$

where

$$\Delta \epsilon_z = |\epsilon_z t_1 T^{-1} - \epsilon_z t_2 T^{-1}|. \quad (3)$$

Additionally, the distance computation can be performed with respect to a specific plane in the FOV. For a plane oriented orthogonal to the z axis at position z_t , Δa_{\min} can be reformulated to

$$\Delta a_{\min,z} = \min \left\{ \left| \epsilon_z t_1 T_{\text{Rep}}^{-1} - z_t \right|, \left| \epsilon_z t_2 T_{\text{Rep}}^{-1} - z_t \right| \right\}. \quad (4)$$

The calculation of the maximal distances follows accordingly. Since the distances $\Delta a_{\min,z}$ are only calculated at the positions of the SIPs, a suitable representation of $\Delta a_{\min,z}$ as a distance map can be generated by use of an interpolation, such as a linear or a polynomial approach, of the calculated distances [29].

Euclidean Distances

In [23], it was proposed to use euclidean distances as an alternative to the aforementioned axial ones. The minimal euclidean distance of a specific point p in a given FOV to the elongated trajectory is defined as

$$\Delta e_{\min} = \min \|\gamma(t) - p\|_2. \quad (5)$$

Again, the calculation of the maximal distances follows accordingly. Corresponding distance maps are based on the cell-centered position of each voxel in the observed plane at position k_t .

III.III. Analysis Techniques

The influence of the data acquisition by an elongated trajectory on the reconstructed images is analyzed within the imaging plane as well as orthogonal to this plane.

A first estimation of potential influences can be made independently of the used data set and only based on the minimal axial and euclidean distances of the elongated trajectory to the plane of interest [21, 23].

For a more detailed characterization of the image quality, the occurrence of distortions in the reconstructed images of the simulation phantom shown in Fig. 2 (a) is analyzed. An elegant way to define the directions of

the largest and the smallest distortion for each reconstructed circle is provided by a principle component analysis (PCA) [31]. Based on a 2D point cloud, the PCA approach allows for the determination of the directions $\mathbf{d}_{\max}, \mathbf{d}_{\min} \in \mathbb{R}^2$ of the principal components with the largest and smallest variance $v_{\max}, v_{\min} \in \mathbb{R}$. To calculate the 2D point cloud for each circle, a threshold based approach is applied [32]. Each pixel coordinate with a gray value larger or equal to the threshold is assigned to the point cloud.

Based on the PCA approach, line profiles in the direction of \mathbf{d}_{\max} and \mathbf{d}_{\min} can be analyzed as a function of the elongation length. In this context, the ratio of the variances v_{\max} and v_{\min} provides a quantitative measure to evaluate the strength of distortion.

Additionally, the PCA method allows an analysis of the relationship between the direction of the largest distortion \mathbf{d}_{\max} in the reconstructed image and the direction of the sampling path. In particular, it can be determined if \mathbf{d}_{\max} is always orthogonal to the FFP path and whether the findings align with the theoretical basis described in [25]. The center of each circle in Fig. 2 (a) corresponds to an SIP of the non-elongated Lissajous trajectory. Thus, there are two positions on the elongated trajectory at the time points t_1 and t_2 with a defined axial distance to the center position of the circle. Based on the time point $t_i, i \in \{1, 2\}$ with the smaller axial distance, the FFP velocity vector $\dot{\mathbf{r}}_{FFP}(t_i) = (\dot{r}_x(t_i), \dot{r}_y(t_i), \dot{r}_z(t_i))^T$ is calculated. Since only distortions in the xy plane are considered, this vector is then projected into the imaging plane. With the resulting 2D direction vector $\tilde{\mathbf{r}}_{FFP}(t_i) = (\dot{r}_x(t_i), \dot{r}_y(t_i))^T$, the intersection angle φ between \mathbf{d}_{\max} and the direction vector of the trajectory $\tilde{\mathbf{r}}_{FFP}(t_i)$ is then calculated by

$$\varphi = \cos^{-1} \left(\frac{\langle \mathbf{d}_{\max}, \tilde{\mathbf{r}}_{FFP}(t_i) \rangle}{\|\mathbf{d}_{\max}\|_2 \|\tilde{\mathbf{r}}_{FFP}(t_i)\|_2} \right). \quad (6)$$

IV. Results

The reconstruction results that serve as a basis for the studies on signal loss and artifacts are shown in Fig. 3. Focusing only on the visual impression of the reconstructions, it becomes apparent that the reconstructed circles are differing for each elongation length. Particular differences appear in the intensity of the reconstructed particle accumulations and the extent as well as the direction of distortion artifacts. Both effects increase with longer elongation. For each elongation, the best results appear to be reconstructed for the circle in the middle and the worst results for the circles in the top right and bottom left corner of the phantom.

The aforementioned observations for the circles can be confirmed by the corresponding intensity profiles in the z direction (see Fig. 4). In terms of the different elon-

gation lengths, the reconstructed intensity values change the least for the circles along the main diagonal. The biggest influence of the elongation on the intensity values can be seen for the circles in the top right and bottom left corner. In addition to this, it is interesting to see that the extent of the blurring in the z direction remains within the interval $[-1X_s G_z^{-1}, 1X_s G_z^{-1}]$ for each of the examined elongation lengths as well as the different circle positions.

Furthermore, the observed differences with respect to the reconstructed particle accumulations and the corresponding signal intensities coincide with the calculated axial and euclidean distances $\Delta a_{\min,z}$ and $\Delta e_{\min,z}$ shown in Fig. 5. In addition to the distance maps, the trajectory segments within and adjacent to the chosen imaging plane are visualized.

It can be seen that for both, the euclidean and the axial distances, similar results can be achieved that also match the observations based on the reconstructions in Fig. 3 and the intensity profiles in Fig. 4. The calculated distances are shorter for small elongation lengths than larger ones. Based on the path of the elongated Lissajous trajectory, the shortest distances between trajectory and imaging plane are along the main diagonal. The distances increase towards the top right and the bottom left corner. This means that based on the distance maps, the distortions of the reconstructed circles in these areas (see Fig. 3) can be directly linked to the trajectory's distance to the imaging plane.

The distortions seen in the reconstruction, especially in the top right and bottom left corners, for elongations larger than $1X_s G_z^{-1}$ may be also related to a violation of the theoretical limits mentioned in Sec. II. In this context, it was also mentioned that the potential occurrence of distortions would be primarily orthogonal to the trajectory. Based on the course of the trajectory shown in Fig. 5, it seems like that a first visual inspection of the results shows a good resemblance. The segments of the trajectory within the imaging plane and also the ones next to it coincide well with the theoretical assumptions regarding the distortion direction. A respective quantitative analysis is performed by use of a PCA and the results are shown in Fig. 6. In Fig. 6 (a), the angles between the movement direction of the FFP and the direction of the largest distortion are illustrated. The determined angles show a good correlation to the theory, because they are all almost orthogonal.

Additionally, in order to get an idea about the ratio of the distortions in \mathbf{d}_{\max} and \mathbf{d}_{\min} , the ratios between the square roots of v_{\max} and v_{\min} are visualized in Fig. 6 (b). Here, the mean differences between the distortions are about 1.13 for $1X_s G_z^{-1}$ and 1.47 for $4X_s G_z^{-1}$. These numbers confirm the theoretical assumptions in Sec. II that in order to prohibit such artifacts, the elongation lengths should not only be limited to $2X_s G_z^{-1}$, but rather to $1X_s G_z^{-1}$.

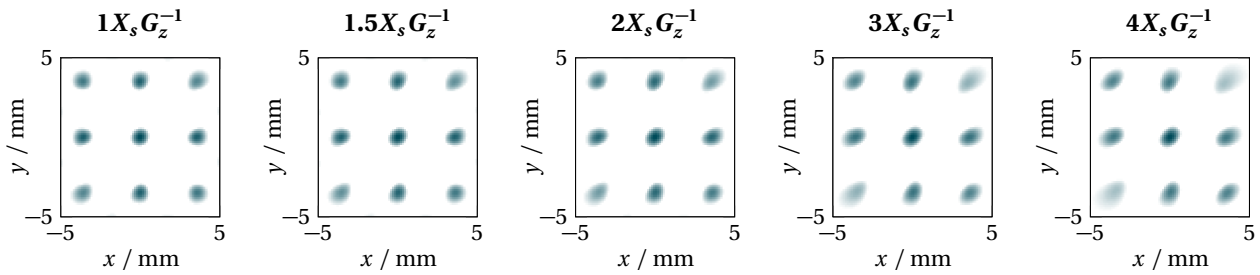


Figure 3: Visualization of the reconstruction results for different elongation lengths. The intensity values are scaled in the range [0, 1].

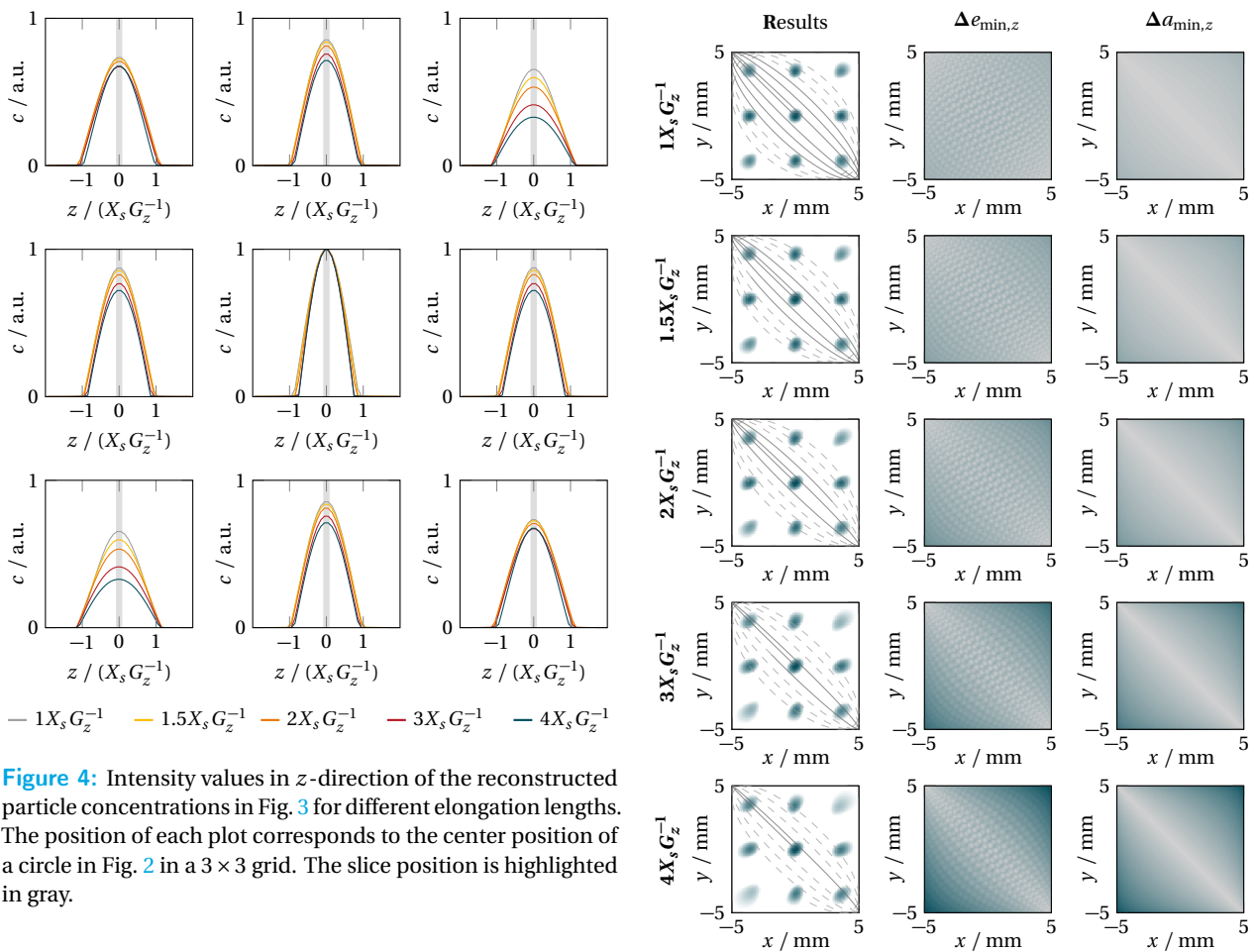


Figure 4: Intensity values in z -direction of the reconstructed particle concentrations in Fig. 3 for different elongation lengths. The position of each plot corresponds to the center position of a circle in Fig. 2 in a 3×3 grid. The slice position is highlighted in gray.

A thorough analysis of the line profiles in the directions of \mathbf{d}_{\max} and \mathbf{d}_{\min} is shown for selected circles in Fig. 7. The intensities are again calculated for each of the considered elongation lengths of this simulation study and presented in comparison to the actual diameter and intensity of the circles from the phantom shown in Fig. 2 (a).

It can be seen that the width of the line profiles in the direction of \mathbf{d}_{\max} increases with an increasing elongation length. The corresponding reconstructed signal intensities change accordingly and decrease for almost each circle, when the trajectory elongation is increased. The

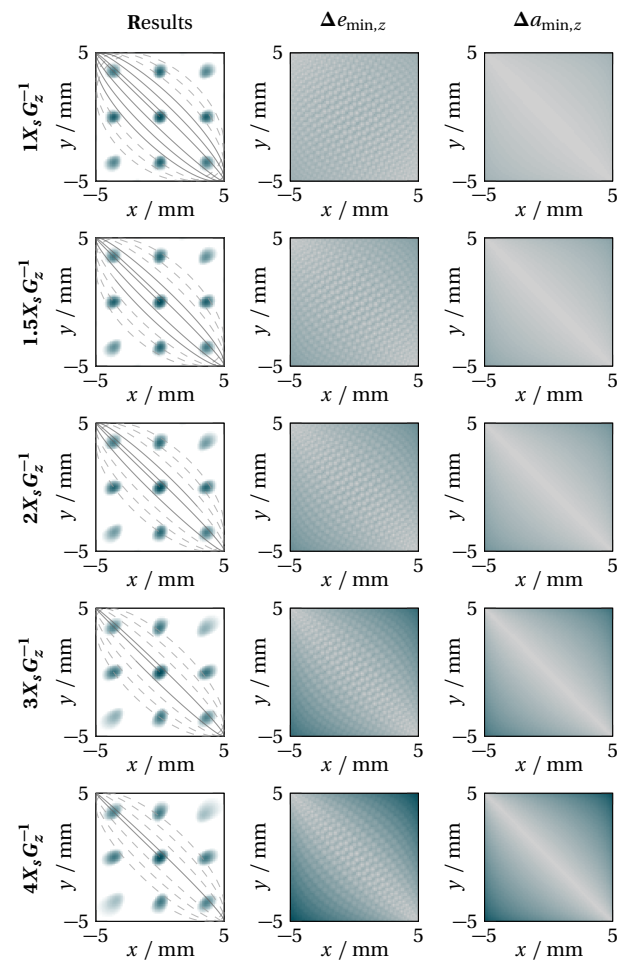


Figure 5: Reconstruction results and distance maps for changing elongation lengths. The reconstructed particle accumulations are superimposed with a visualization of the trajectory segments in the reconstructed slice (gray, solid) and the neighboring slices (gray, dashed). The images are scaled in the range [0, 1]. The distance maps based on $\Delta a_{\min,z}$ are created using linear interpolation.

only exception is given by the middle circle, where the intensity values remain nearly constant. The line profiles along the main diagonal are close to be axisymmetrical.

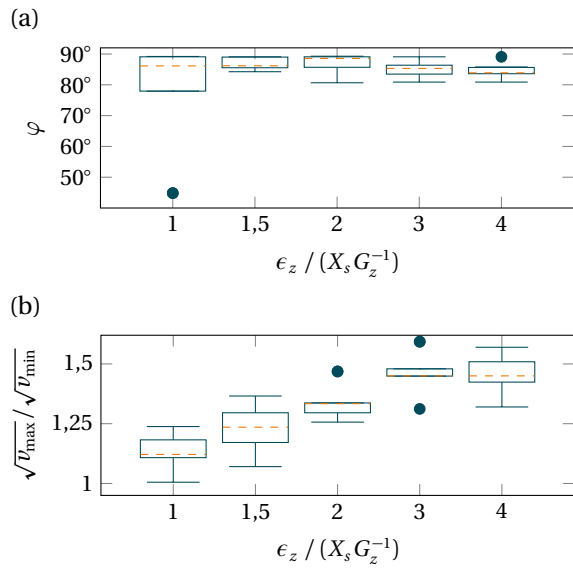


Figure 6: PCA based results of the distortion determination visualized as boxplots. The box (green) represents the values within the upper and lower quartiles around the median (orange, dashed). Additionally, the entire range of values (green, lines) and outliers (green, circles) are specified. (a) Calculated angle values φ between the direction of the largest distortion and the direction of the FFP movement at each circle center. (b) Ratio between the square roots of v_{\max} and v_{\min} .

With an increasing distance to the main diagonal, the intensity profiles become increasingly distorted towards the diagonal. In the direction of d_{\min} , the line profiles are all almost axisymmetrical and no significant variance in terms of the width for the different elongations can be observed. According to the findings for the profiles in the direction of d_{\max} , the intensities for the middle circles are constant, while the intensities for the other circle vary.

V. Discussion

In order to further understand potentially occurring artifacts caused by the use of an elongated data acquisition in MPI, a simulation based analysis has been carried out.

It was shown that both the euclidean and the axial distance are suitable measures to determine the distance of a trajectory to an imaging plane. The results confirm the assumption that these distances are in a direct correlation to a loss in signal intensity as well as the occurrence of distortion artifacts. A further consideration of the actual course of the trajectory within and adjacent to the imaging plane confirms these findings as well. An interesting extension for the distance calculation would be the inclusion of the particles point spread function or the decreasing course of potential signal intensities.

The direction of the largest distortion was analyzed

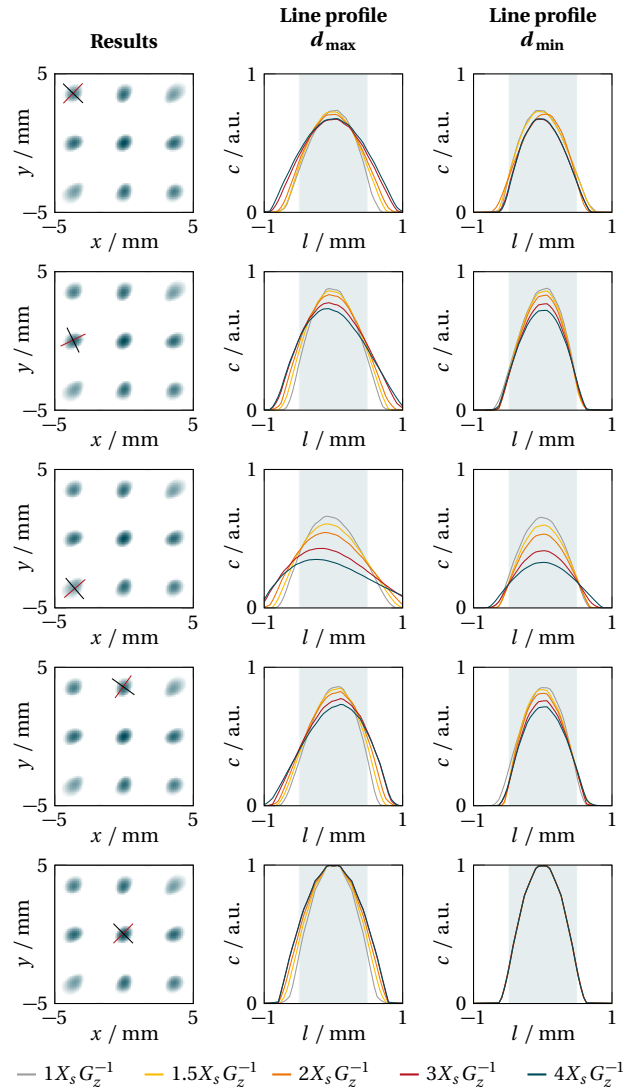


Figure 7: Visualization of the line profiles in the direction of d_{\max} (red) and d_{\min} (black) given by a length parameter l . The profiles are shown for the elongation lengths $1X_s G_z^{-1}$, $1.5X_s G_z^{-1}$, $2X_s G_z^{-1}$, $3X_s G_z^{-1}$ and $4X_s G_z^{-1}$. The diameter and the signal intensity of the circles from Fig. 2 are highlighted.

for each circle of the used simulation phantom based on a PCA. The PCA results showed that the largest distortion appears to be always nearly orthogonal to the path of the Lissajous trajectory. Since the appearance of the distortion seems to be rather independent of the used phantom, it would be interesting to see, if there is a possibility of creating a distortion map for a chosen trajectory which could be used as a regularization during the reconstruction or maybe already during the acquisition process.

In order to fully understand the effects caused by an elongated data acquisition path and to validate the theoretical assumptions, further experiments with different 3D phantoms and especially the use of measured MPI

data is mandatory. The related effects caused by the used MPI system or the particle dynamics would influence the results significantly and it is unclear, if new artifacts could be introduced by this or if the theoretical assumptions are already sufficient for real measurement scenarios.

VI. Conclusion

In this work, a detailed simulation based analysis of the possibility of signal loss and the occurrence of distortion artifacts has been carried out in the context of elongated trajectories in MPI. A Lissajous trajectory was chosen as a data acquisition path and a phantom was positioned in the middle of the FOV in z direction as an example imaging plane. It should be mentioned that the shown results for this imaging plane can be transferred to any arbitrarily positioned plane in the FOV. Based on the shown correlation to the data acquisition path, the respective acquired signal intensities and the directions of the distortion artifacts would change accordingly to the plane position. As tools for the analysis, a determination of the axial and euclidean minimal distances to the imaging plane and a PCA were used. Both approaches could be used to further explain the reconstruction results achieved with an elongated trajectory. An important information for the use of such a trajectory is that the occurrence of artifacts can be reduced significantly, when the elongation length is limited to $1X_s G_z^{-1}$.

Acknowledgment

The authors gratefully acknowledge the financial support of the German Research Foundation (DFG, grant number BU 1436/9-1).

References

- [1] B. Gleich and J. Weizenecker. Tomographic imaging using the nonlinear response of magnetic particles. *Nature*, 435(7046):1214–1217, 2005. doi:[10.1038/nature03808](https://doi.org/10.1038/nature03808).
- [2] J. Weizenecker, B. Gleich, J. Rahmer, H. Dahnke, and J. Borgert. Three-dimensional real-time in vivo magnetic particle imaging. *Phys. Med. Biol.*, 54(5):L1–L10, 2009.
- [3] J. Haegele, J. Rahmer, B. Gleich, J. Borgert, H. Wojtczyk, N. Panagiotopoulos, T. M. Buzug, J. Barkhausen, and F. M. Vogt. Magnetic Particle Imaging: Visualization of Instruments for Cardiovascular Intervention. *Radiology*, 265(3):933–938, 2012.
- [4] J. Rahmer, A. Antonelli, C. Sfara, B. Tiemann, B. Gleich, M. Magnani, J. Weizenecker, and J. Borgert. Nanoparticle encapsulation in red blood cells enables blood-pool magnetic particle imaging hours after injection. *Phys. Med. Biol.*, 58(12):3965, 2013. doi:[10.1088/0031-9155/58/12/3965](https://doi.org/10.1088/0031-9155/58/12/3965).
- [5] B. Zheng, T. Vazin, P. W. Goodwill, A. Conway, A. Verma, E. U. Saritas, D. Schaffer, and S. M. Conolly. Magnetic Particle Imaging tracks the long-term fate of in vivo neural cell implants with high image contrast. *Sci. Rep.*, 5:14055, 2015. doi:[10.1038/srep14055](https://doi.org/10.1038/srep14055).
- [6] N. Panagiotopoulos, R. L. Duschka, M. Ahlborg, G. Bringout, C. Debbeler, M. Graeser, C. Kaethner, K. Lüdtkke-Buzug, H. Medimagh, J. Stelzner, T. M. Buzug, J. Barkhausen, F. M. Vogt, and J. Haegele. Magnetic particle imaging: current developments and future directions. *Int. Journ. Nanomed.*, 10:3097, 2015. doi:[10.2147/IJN.S70488](https://doi.org/10.2147/IJN.S70488).
- [7] J. Salamon, M. Hofmann, C. Jung, M. G. Kaul, F. Werner, K. Them, R. Reimer, P. Nielsen, A. vom Scheidt, G. Adam, T. Knopp, and H. Ittrich. Magnetic Particle / Magnetic Resonance Imaging: In-Vitro MPI-Guided Real Time Catheter Tracking and 4D Angioplasty Using a Road Map and Blood Pool Tracer Approach. *PLOS ONE*, 11(6):e0156899, 2016. doi:[10.1371/journal.pone.0156899](https://doi.org/10.1371/journal.pone.0156899).
- [8] P. Vogel, M. A. Rückert, P. Klauer, W. H. Kullmann, P. M. Jakob, and V. C. Behr. First in vivo traveling wave magnetic particle imaging of a beating mouse heart. *Phys. Med. Biol.*, 61(18):6620–6634, 2016. doi:[10.1088/0031-9155/61/18/6620](https://doi.org/10.1088/0031-9155/61/18/6620).
- [9] T. F. Sattel, T. Knopp, S. Biederer, B. Gleich, J. Weizenecker, J. Borgert, and T. M. Buzug. Single-sided device for magnetic particle imaging. *J. Phys. D: Appl. Phys.*, 42(1):1–5, 2009. doi:[10.1088/0022-3727/42/2/022001](https://doi.org/10.1088/0022-3727/42/2/022001).
- [10] P. Vogel, S. Lother, M.A. Ruckert, W.H. Kullmann, P.M. Jakob, F. Fidler, and V.C. Behr. MRI Meets MPI: A Bimodal MPI-MRI Tomograph. *IEEE Trans. Med. Imag.*, 33(10):1954–1959, 2014. doi:[10.1109/TMI.2014.2327515](https://doi.org/10.1109/TMI.2014.2327515).
- [11] J. Rahmer, A. Halkola, B. Gleich, I. Schmale, and J. Borgert. First experimental evidence of the feasibility of multi-color magnetic particle imaging. *Phys. Med. Biol.*, 60(5):1775–1791, 2015. doi:[10.1088/0031-9155/60/5/1775](https://doi.org/10.1088/0031-9155/60/5/1775).
- [12] J. Weizenecker, B. Gleich, and J. Borgert. Magnetic particle imaging using a field free line. *J. Phys. D: Appl. Phys.*, 41(10):105009, 2008. doi:[10.1088/0022-3727/41/10/105009](https://doi.org/10.1088/0022-3727/41/10/105009).
- [13] T. Knopp, M. Erbe, S. Biederer, T. F. Sattel, and T. M. Buzug. Efficient generation of a magnetic field-free line. *Med. Phys.*, 37(7):3538–3540, 2010. doi:[10.1118/1.3447726](https://doi.org/10.1118/1.3447726).
- [14] K. Bente, M. Weber, M. Graeser, T. F. Sattel, M. Erbe, and T. M. Buzug. Electronic field free line rotation and relaxation deconvolution in magnetic particle imaging. *IEEE Trans. Med. Imag.*, 34(2):644–651, 2015. doi:[10.1109/TMI.2014.2364891](https://doi.org/10.1109/TMI.2014.2364891).
- [15] P. W. Goodwill, E. U. Saritas, L. R. Croft, T. N. Kim, K. M. Krishnan, D. V. Schaffer, and S. M. Conolly. X-Space MPI: Magnetic Nanoparticles for Safe Medical Imaging. *Adv. Mater.*, 24:3870–3877, 2012. doi:[10.1002/adma.201200221](https://doi.org/10.1002/adma.201200221).
- [16] T. Knopp, S. Biederer, T. Sattel, J. Weizenecker, B. Gleich, J. Borgert, and T. M. Buzug. Trajectory analysis for magnetic particle imaging. *Phys. Med. Biol.*, 54(2):385–397, 2009. doi:[10.1088/0031-9155/54/2/014](https://doi.org/10.1088/0031-9155/54/2/014).
- [17] J. P. Reilly. Magnetic field excitation of peripheral nerves and the heart: a comparison of thresholds. *Med. Biol. Eng. Comput.*, 29(6):571–579, 1991.
- [18] E. U. Saritas, P. W. Goodwill, G. Z. Zhang, and S. M. Conolly. Magnetostimulation Limits in Magnetic Particle Imaging. *IEEE Trans. Med. Imag.*, 32(9):1600–1610, 2013. doi:[10.1109/TMI.2013.2260764](https://doi.org/10.1109/TMI.2013.2260764).
- [19] O. Doessel and J. Bohnert. Safety considerations for magnetic fields of 10 mT to 100 mT amplitude in the frequency range of 10 kHz to 100 kHz for magnetic particle imaging. *Biomed. Tech. / Biomed. Eng.*, 58(6):611–621, 2013. doi:[10.1515/bmt-2013-0065](https://doi.org/10.1515/bmt-2013-0065).
- [20] I. Schmale, J. Rahmer, B. Gleich, J. Kanzenbach, J. D. Schmidt, C. Bontus, O. Woywode, and J. Borgert. First phantom and in vivo MPI images with an extended field of view. In *SPIE Medical Imaging*, 2011. doi:[10.1117/12.877339](https://doi.org/10.1117/12.877339).
- [21] C. Kaethner, M. Ahlborg, G. Bringout, M. Weber, and T. M. Buzug. Axially Elongated Field-Free Point Data Acquisition in Magnetic Particle Imaging. *IEEE Trans. Med. Imag.*, 34(2):381–387, 2015. doi:[10.1109/TMI.2014.2357077](https://doi.org/10.1109/TMI.2014.2357077).
- [22] P. Vogel, M. A. Rückert, P. Klauer, W. H. Kullmann, P. M. Jakob, and V. C. Behr. Rotating Slice Scanning Mode for Traveling Wave Magnetic Particle Imaging. *IEEE Trans. Magn.*, 51(2):6501503,

2015. doi:[10.1109/TMAG.2014.2335255](https://doi.org/10.1109/TMAG.2014.2335255).
- [23] A. Haensch, C. Kaethner, A. Cordes, and T. M. Buzug. Towards the Characterization of Distortion Artifacts in Elongated Trajectory MPI. In *International Workshop on Magnetic Particle Imaging*, page 114, 2016.
- [24] B. Gleich. *Principles and Applications of Magnetic Particle Imaging*. Springer Vieweg, Wiesbaden, 2014.
- [25] P. W. Goodwill and S. M. Conolly. Multidimensional X-Space Magnetic Particle Imaging. *IEEE Trans. Med. Imag.*, 30(9):1581–1590, 2011.
- [26] A. Cordes, C. Kaethner, M. Ahlborg, and T. M. Buzug. X-space Deconvolution for Multidimensional Lissajous-based Data- Acquisition Schemes. In *International Workshop on Magnetic Particle Imaging (IWMPI) 2016, Book of Abstracts*, page 74, 2016.
- [27] J. Weizenecker, B. Gleich, and J. Borgert. A simulation study on the resolution and sensitivity of magnetic particle imaging. *Phys. Med. Biol.*, 52(21):6363–6374, 2007. doi:[10.1088/0031-9155/52/21/001](https://doi.org/10.1088/0031-9155/52/21/001).
- [28] W. Erb, C. Kaethner, M. Ahlborg, and T. M. Buzug. Bivariate Lagrange interpolation at the node points of non-degenerate Lissajous curves. *Numer. Math.*, 133(4):685–705, 2016. doi:[10.1007/s00211-015-0762-1](https://doi.org/10.1007/s00211-015-0762-1).
- [29] W. Erb, C. Kaethner, P. Denker, and M. Ahlborg. A survey on bivariate Lagrange interpolation on Lissajous nodes. *DRNA*, 8:23–36, 2015. doi:[10.14658/pupj-drna-2015-Special_Issue-4](https://doi.org/10.14658/pupj-drna-2015-Special_Issue-4).
- [30] A. Dax. On row relaxation methods for large constrained least squares problems. *SIAM J. Sci. Comput.*, 14(3):570–584, 1993. doi:[10.1137/0914036](https://doi.org/10.1137/0914036).
- [31] G. Dougherty. *Pattern Recognition and Classification: An Introduction*. Springer Verlag, New York, 2013. doi:[10.1007/978-1-4614-5323-9](https://doi.org/10.1007/978-1-4614-5323-9).
- [32] N. Otsu. A Threshold Selection Method from Gray-Level Histograms. *IEEE Trans. Syst., Man, Cybern., Syst.*, 9(1):62–66, 1979. doi:[10.1109/TSMC.1979.4310076](https://doi.org/10.1109/TSMC.1979.4310076).